

Vector-based elastic reverse time migration based on scalar imaging condition

Qizhen Du¹, ChengFeng Guo¹, Qiang Zhao¹, Xufei Gong¹,
Chengxiang Wang², and Xiang-yang Li³

ABSTRACT

The scalar images (PP, PS, SP, and SS) of elastic reverse time migration (ERTM) can be generated by applying an imaging condition as crosscorrelation of pure wave modes. In conventional ERTM, Helmholtz decomposition is commonly applied in wavefield separation, which leads to a polarity reversal problem in converted-wave images because of the opposite polarity distributions of the S-wavefields. Polarity reversal of the converted-wave image will cause destructive interference when stacking over multiple shots. Besides, in the 3D case, the curl calculation generates a vector S-wave, which makes it impossible to produce scalar PS, SP, and SS images with the crosscorrelation imaging condition. We evaluate a vector-based ERTM (VB-ERTM) method to

address these problems. In VB-ERTM, an amplitude-preserved wavefield separation method based on decoupled elastic wave equation is exploited to obtain the pure wave modes. The output separated wavefields are both vectorial. To obtain the scalar images, the scalar imaging condition in which the scalar product of two vector wavefields with source-normalized illumination is exploited to produce scalar images instead of correlating Cartesian components or magnitude of the vector P- and S-wave modes. Compared with alternative methods for correcting the polarity reversal of PS and SP images, our ERTM solution is more stable and simple. Besides these four scalar images, the VB-ERTM method generates another PP-mode image by using the auxiliary stress wavefields. Several 2D and 3D numerical examples are evaluated to demonstrate the potential of our ERTM method.

INTRODUCTION

Because the wavefield is reconstructed using the two-way wave equation, reverse time migration (RTM) (Baysal et al., 1983; McMechan, 1983; Whitmore, 1983) provides a natural way to deal with the primary reflections and other complex waves, such as refractions, multiple reflections, and prismatic waves, and it imposes no dip limitations on the images. These complex wave modes allow imaging subsurfaces that have poor direct illumination. At present, RTM is an important method for imaging complex subsurface structures (Yoon et al., 2003; Yoon and Marfurt, 2006; Fletcher et al., 2009; Zhang et al., 2011). In the past several years, multicomponent seismic exploration has drawn more and more attention for its advantages in reservoir monitoring, hydrocarbons detection, and lithological discrimination (Stewart et al., 2003; Du et al., 2012). And,

multicomponent elastic RTM (ERTM) has been one of focuses in multicomponent seismic data processing.

Conventional acoustic RTM consists of two steps: (1) constructing a source wavefield in a given velocity model using an estimated wavelet and (2) propagating the recorded data downward through the same velocity model into the earth and applying an imaging condition (Claerbout, 1971). Elastic RTM follows the same procedures. For multicomponent seismic data, early attempts of ERTM were based on the Cartesian component imaging algorithms (Chang and McMechan, 1986, 1994), which crosscorrelates the Cartesian components of the vector wavefields. However, in their component imaging algorithm, these migrated results from horizontal or vertical components lead to an unclear physical meaning and exhibited artifacts caused by crosstalk between the unseparated wave modes (Yan and Sava, 2008).

Manuscript received by the Editor 17 March 2016; revised manuscript received 30 November 2016; published online 17 February 2017.

¹China University of Petroleum (East China), School of Geosciences, Qingdao, China. E-mail: multicomponent@163.com; guo_chengfeng@163.com; zq_clark@163.com; gong_xufei@126.com.

²BGP, CNPC, Zhuozhou, China. E-mail: wangchengxiang126@126.com.

³China University of Petroleum, Beijing, China. E-mail: xyl@bgs.ac.uk.

© 2017 Society of Exploration Geophysicists. All rights reserved.

To avoid crosstalk artifacts and provide images with more clear physical meaning, elastic RTM algorithm for scalar images (i.e., PP, PS, SP, and SS images) constructed with pure wave modes (P- and S-waves) is proposed. There are mainly two approaches for multi-component data to obtain meaningful scalar images: scalar and elastic frameworks. The scalar migration framework, ignoring the intrinsic elastic property of the vector wavefield, requires multi-component seismic data to be separated into P- and S-waves before applying the scalar RTM of P- and S-waves independently (Sun and McMechan, 2001; Sun et al., 2006). Though the scalar migration framework makes full use of mature acoustic RTM technology, it cannot correctly cope with the converted energy. In elastic frameworks, on the contrary, the elastic source and receiver wavefields are constructed with the elastic wave equation. Unlike the Cartesian component imaging algorithm, before applying the imaging condition, the elastic wavefields are commonly first separated into P- and S-waves, for example, using Helmholtz decomposition. Then, the scalar images are extracted by applying the imaging condition to P- and S-waves of the source and receiver wavefields. Each of the migrated images describes the reflectivity of a specified reflection mode, which is easier to interpret (Yan and Sava, 2008). However, the PS- and SP-wave images resulting from this method undergo polarity reversal that will lead to destructive interference when stacking, which requires additional polarity correction methods (Balch and Erdemir, 1994; Du et al., 2012). Furthermore, in the 3D case, Helmholtz decomposition will generate a 3C vector S-wave, which makes it impossible to generate a scalar PS image with the conventional crosscorrelation imaging condition. Some researchers use S-wave scalarization (Du et al., 2014) or modify the imaging condition (Duan and Sava, 2015) to obtain scalar images. Considering the issue of polarity reversal and the fact that several images for different wave modes are difficult to interpret, a brand-new elastic wavefield imaging condition based on the energy norm is developed (Rocha et al., 2016). This energy imaging condition does not need wave-mode decomposition, it combines all wave modes into a single image, and it is free from polarity reversal. But the potential cost of this alternative (combining all wave modes into a single image) is that the hidden geophysical information of S-wave data cannot be fully excavated. So in this paper, we still focus our work on the PP and PS images' ERTM framework.

In our study, we found that the polarity correction method for converted-wave images is not accurate enough in complex subsurface geologic structures that contain a high-contrast discontinuous interface. Complex discontinuous interfaces lead to inaccuracy in calculating the sign factor of the S-wave. One possibility to overcome this problem is to set up an elastic RTM algorithm in which the polarity reversal problem does not exist at all rather than to correct it using the Poynting vectors (Červený, 2001; Yoon and Martfurt, 2004, 2006) or the relationships among incident and reflected wave directions (Duan and Sava, 2015).

Recently, elastic RTM algorithms based on the so-called decoupled P- and S-wave equations (Ma and Zhu, 2003) are proposed. From the Helmholtz decomposition theory that a vector wavefield can be decomposed into a curl-free P-wave part and a divergence-free S-wave part (Aki and Richards, 1980), Ma and Zhu (2003) give an equivalent displacement equation of full elastic equation allowing P- and S-waves to propagate separately in an elastic medium. Later, following Ma and Zhu (2003), Li et al. (2007)

and Zhang et al. (2007) further develop 2D decoupled P- and S-wave stress-velocity formulations. Xiao and Leaney (2010) also propose decoupled P- and S-wave equations, in which the auxiliary P- and S-wave stresses are introduced to attain the P- and S-wave wavefields. The introduction of auxiliary P- and S-wave stresses makes the decoupled wave equation mathematically simpler, more physically meaningful, and compatible with conventional elastic wave equation. Based on the separation method, they further develop a local vertical seismic profiling elastic RTM for transmitted P-to-S-waves, in which a scalar imaging condition is used to produce the scalar PS image. Following Xiao and Leaney (2010), Wang and McMechan (2015) propose a new 2D elastic RTM method, in which the magnitude of the receiver particle-velocity wavefield is divided by the source wavefield, and the P- and S-wave Poynting vectors are exploited to determine the corresponding sign of the reflection coefficient. Shabelansky et al. (2015) use a similar separation method in source-independent converted-wave elastic migration velocity analysis, and develop an extended space-shift converted-wave imaging condition in which the scalar product of the receiver P- and S-wave vectors is used to produce a source-independent polarity-consistent PS image. Gu et al. (2015) use a similar idea to separate the P- and S-waves, but the components of the P- and S-wave particle velocities are crosscorrelated in their elastic RTM algorithm.

The main advantage of the decoupled wave equation is that amplitude and phase are accurately preserved. Compared with the pure wavefields from Helmholtz decomposition, the outputs of the decoupled wave equation are more physically meaningful. In this paper, we propose an alternative, stable and simple, vector-based ERTM (VB-ERTM) method for multicomponent seismic data based on the decoupled wave equation. It does not need geometric relationships among the source and receiver wavefields and the reflector orientation like the method proposed by Duan and Sava (2015), nor do we need to calculate the sign of the reflection coefficients like the method proposed by Wang and McMechan (2015). These additional calculations may bring inaccuracy and errors in complicated models. In our VB-ERTM, not only are the particle velocity wavefields considered, but also the stress wavefields. The paper is organized as follows: First, the equations used to model pure P- and S-waves are briefly reviewed. Second, a source-normalized scalar-product-based imaging condition for vector wavefields is introduced to generate scalar images. Third, the possibility of crosscorrelating the auxiliary P-wave stress to produce a scalar PP image is discussed. And last, 2D and 3D numerical examples on simple and complex models are used to demonstrate the potential of the proposed method.

METHODOLOGY

Decoupled P- and S-wave equations

The elastic wave equation in an infinite, homogeneous, isotropic medium is (Aki and Richards, 1980)

$$\rho \ddot{\mathbf{u}} = (\lambda + 2\mu) \nabla (\nabla \cdot \mathbf{u}) - \mu \nabla \times \nabla \times \mathbf{u}, \quad (1)$$

where \mathbf{u} is the displacement vector wavefield, $\ddot{\mathbf{u}}$ is the second-order time derivative of the displacement vector wavefield, ρ is the density, and λ and μ are the Lamé moduli. Here, ∇ , $\nabla \cdot$, and $\nabla \times$ are the gradient, divergence, and curl, respectively. For the isotropic case, a

vector wavefield can be separated into a curl-free P-wave part and a divergence-free S-wave part; i.e.

$$\mathbf{u} = \mathbf{u}^P + \mathbf{u}^S, \quad (2)$$

with

$$\nabla \times \mathbf{u}^P = 0 \quad (3)$$

and

$$\nabla \cdot \mathbf{u}^S = 0. \quad (4)$$

Equations (2–4) indicate two wavefield separation methods. The first way is applying the divergence and curl operators to the extrapolated elastic wavefields (Dellinger and Etgen, 1990). The output results are the scalar P-wave and the vector S-wave. In the 2D case, the S-wave has only one component, and we can reasonably treat it as a scalar, but the S-wave has an opposite sign distribution on the two sides of the normal direction, which requires an additional polarity-reversal correction (Du et al., 2012). Besides, in the 3D case, additional scalarization of the vector S-wave is necessarily required to produce scalar images (Du et al., 2014).

The second approach to obtain P- and S-waves is using equation 2 directly. Zhang and McMechan (2010) detail this separation method in the wavenumber domain. In fact, it can be implemented in the spatial domain. From the Helmholtz decomposition theory, the acceleration of the displacement wavefield can be decomposed as $\ddot{\mathbf{u}} = \ddot{\mathbf{u}}^P + \ddot{\mathbf{u}}^S$, where

$$\ddot{\mathbf{u}}^P = b(\lambda + 2\mu)\nabla(\nabla \cdot \mathbf{u}) \quad (5)$$

and

$$\ddot{\mathbf{u}}^S = -b\mu\nabla \times \nabla \times \mathbf{u}, \quad (6)$$

where $\ddot{\mathbf{u}}^P$ and $\ddot{\mathbf{u}}^S$ represent the decomposed P- and S-wave acceleration wavefields and b is the inverse of density ρ . Shabelansky et al. (2015) recommend using this decomposed method in elastic RTM instead of Helmholtz decomposition to avoid polarity reversal in converted-wave images. Because the decomposition by using equations 5 and 6 is embedded in the update of the displacement wavefield, the decomposition process needs no additional computation and the amplitude and phase are accurately preserved.

If we further combine equations 2, 5, and 6, we then obtain the decoupled P- and S-wave propagation equation (Ma and Zhu, 2003):

$$\begin{cases} \mathbf{u} = \mathbf{u}^P + \mathbf{u}^S, \\ \ddot{\mathbf{u}}^P = b(\lambda + 2\mu)\nabla(\nabla \cdot \mathbf{u}), \\ \ddot{\mathbf{u}}^S = -b\mu\nabla \times \nabla \times \mathbf{u}. \end{cases} \quad (7)$$

By solving equation 7, the separated P- and S-waves characterizing vector displacement of source and receiver wavefields are available for ERTM. And further, we can transform equation 7 to another compact form as shown here

$$\begin{cases} \ddot{\mathbf{u}} = b(\lambda + 2\mu)\nabla(\nabla \cdot \mathbf{u}) - b\mu\nabla \times \nabla \times \mathbf{u}, \\ \ddot{\mathbf{u}}^P = b(\lambda + 2\mu)\nabla(\nabla \cdot \mathbf{u}), \\ \mathbf{u}^S = \mathbf{u} - \mathbf{u}^P. \end{cases} \quad (8)$$

Even though equations 7 and 8 have similar forms, the basic ideas of these two wave equations are different. The basic idea of equation 7 is to establish wave equations for the P- and S-waves, respectively, and to obtain the total wavefield by adding them up, whereas in equation 8, we only need to establish the wave equation for the P-wave and obtain the S-wave by subtracting the P-wave energy from the total wavefield. It is obvious that the second idea to implement a decoupled wave equation is more convenient and more easily applied to other elastic wave equation forms because the P-wave equation is quite simple compared with the S-wave equation. Because S-waves suffer from severe numerical dispersion due to its low velocity, we prefer to use the first-order staggered-grid stress-particle velocity wave equation (Li et al., 2007; Zhang et al., 2007; Xiao and Leaney, 2010; Gu et al., 2015; Wang et al., 2015; Wang and McMechan, 2015) to reduce numerical dispersion instead of equation 8. In our ERTM algorithm, we construct source and receiver wavefields with the implementation strategy proposed by Xiao and Leaney (2010) for its good compatibility to conventional elastic stress-particle velocity wave equation and its physical interpretation. The computations consist of the following procedures:

- 1) Compute the particle velocity $\mathbf{v} = \{v_x, v_y, v_z\}$ and stress tensor $\boldsymbol{\tau} = \{\tau_{xx}, \tau_{yy}, \tau_{zz}, \tau_{yz}, \tau_{xz}, \tau_{xy}\}$ by using a conventional stress-particle velocity wave equation.
- 2) Compute the auxiliary wavefield τ^P by using $\tau^P = (\lambda + 2\mu)\nabla \cdot \mathbf{v}$.
- 3) Compute the P-wave particle-velocity $\mathbf{v}^P = \{v_x^P, v_y^P, v_z^P\}$ by using $v_i^P = b\tau_i^P (i = x, y, z)$.
- 4) Compute the S-wave particle-velocity $\mathbf{v}^S = \{v_x^S, v_y^S, v_z^S\}$ by using $v_i^S = v_i - v_i^P (i = x, y, z)$.

The most additional computational cost, compared with the conventional stress-velocity wave equation, lies in the three distinct spatial derivatives in procedure 3. A non-negligible fact is that in heterogeneous media, the P- and S-waves cannot be completely separated with the decoupled P- and S-waves equation unless the shear modulus and density are constant (see Appendix A). So, to implement this separation method in the ERTM, the shear modulus (or S velocity) and density need to be smoothed to avoid artifacts caused by secondary reflections and mode conversions produced by coupling at the reflectors (Wang and McMechan, 2015).

An equivalent first-order stress-particle velocity decoupled wave equation proposed by Li et al. (2007) is shown in Appendix B. This equivalent decoupled wave equation stems from equation 7. Compared with procedures discussed above, this equivalent decoupled appears more complex especially in 3D case, but it suggests the S-wave stress tensor construction.

Scalar imaging condition for vector wavefields

A drawback of the decoupled P- and S-wave propagation separation method is that the resulting pure modes are both vectors. In those ERTM algorithms (Gu et al., 2015) based on the decoupled P- and S-wave propagation, the coordinate-dependent images constructed by crosscorrelating Cartesian components of pure wave

modes are not in accord with our conventional understanding of reflectivity and may make interpretation difficult.

To address this problem, the scalar imaging conditions for vector pure wave modes are exploited:

$$I_{PP}(\mathbf{x}) = \int_0^{T_{\max}} \mathbf{S}^P(\mathbf{x}, t) \cdot \mathbf{R}^P(\mathbf{x}, t) dt / \int_0^{T_{\max}} \mathbf{S}^P(\mathbf{x}, t) \cdot \mathbf{S}^P(\mathbf{x}, t) dt, \quad (9)$$

Figure 1. Sign distributions of PP (blue) and PS (red) images as the offset changes. The black arrow line represents the forward-time downgoing source P-wave wavefield, the blue arrow line represents the reverse-time upgoing receiver P-wave wavefield, and the red arrow line represents the reverse-time upgoing receiver S-wave wavefield. The PP image amplitude from the dot-product imaging condition implicitly contains a scaling factor $\cos(2\alpha)$, and the PS image amplitude contains $\sin(\alpha + \beta)$, where α is the P-wave incident (reflected) angle and β is the reflected S-wave angle. As the incident angle α increases, the sign of $\cos(2\alpha)$ varies from positive to negative, whereas $\sin(\alpha + \beta)$ keeps the same sign. This indicates that the sign of the PS image is consistent as the offset increases, but the sign of the PP image changes at a certain offset.

$$I_{PS}(\mathbf{x}) = \int_0^{T_{\max}} \mathbf{S}^P(\mathbf{x}, t) \cdot \mathbf{R}^S(\mathbf{x}, t) dt / \int_0^{T_{\max}} \mathbf{S}^P(\mathbf{x}, t) \cdot \mathbf{S}^P(\mathbf{x}, t) dt, \quad (10)$$

$$I_{SP}(\mathbf{x}) = \int_0^{T_{\max}} \mathbf{S}^S(\mathbf{x}, t) \cdot \mathbf{R}^P(\mathbf{x}, t) dt / \int_0^{T_{\max}} \mathbf{S}^S(\mathbf{x}, t) \cdot \mathbf{S}^S(\mathbf{x}, t) dt, \quad (11)$$

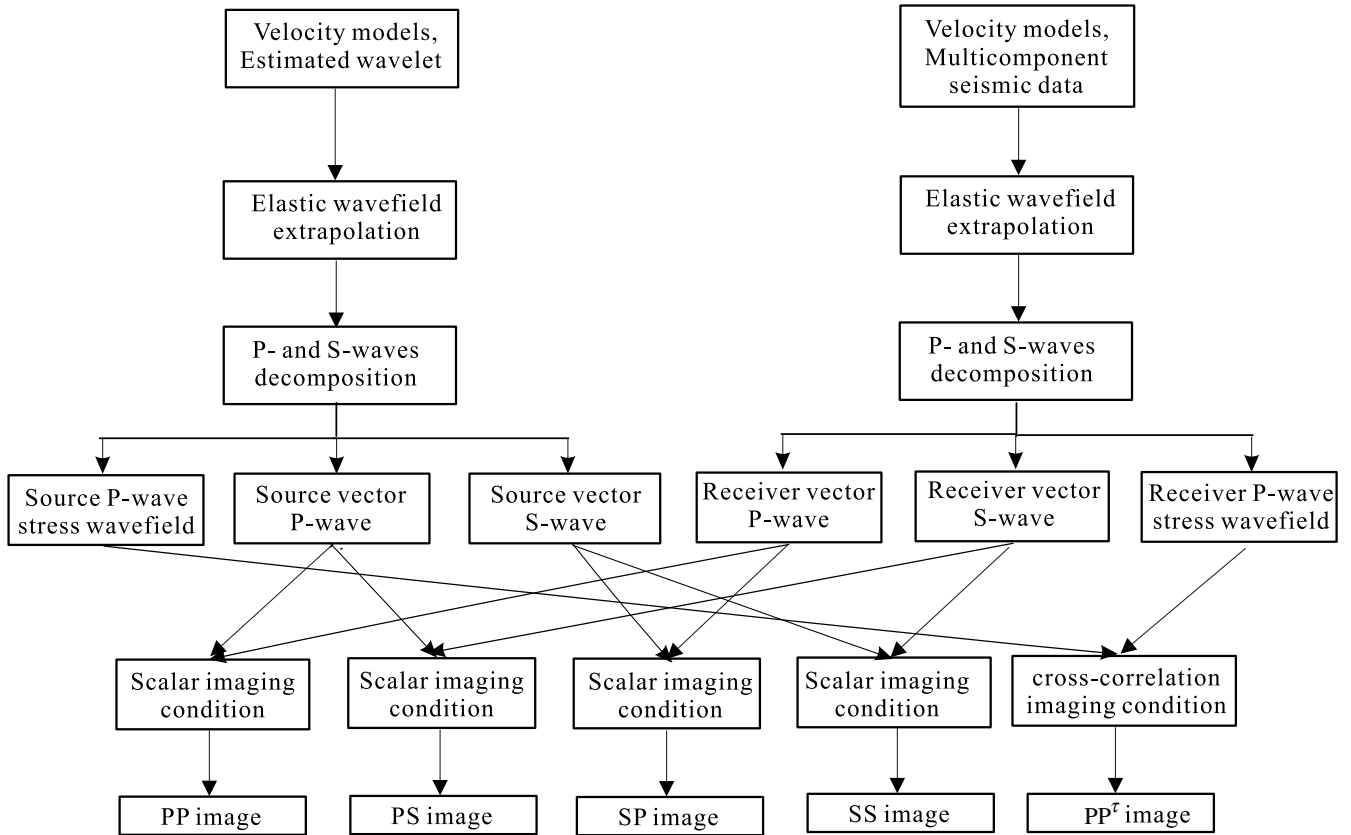
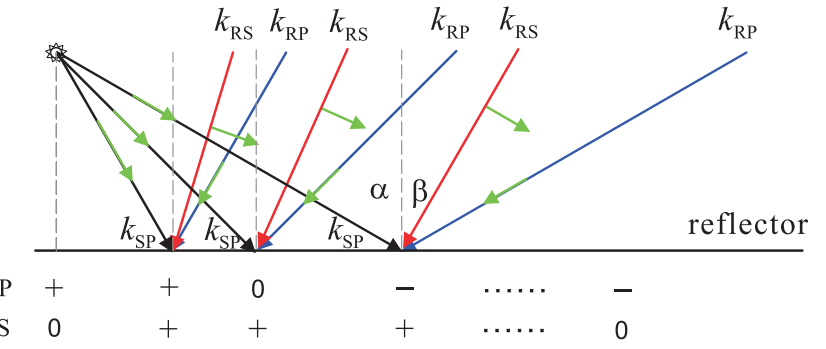


Figure 2. Flow chart of ERTM based on the scalar imaging condition with the vector P- and S-wave wavefields. The source wavefield can be the first to be calculated and saved before receiver wavefield construction, or it can be reconstructed from information generated during a forward source wavefield extrapolation. Theoretically, five scalar images (PP, PS, SP, SS, and PP^r) are produced simultaneously. The P-wave stress image (the PP^r image) can be treated as an auxiliary image or an alternative replacement of the PP image due to its better properties.

$$I_{SS}(\mathbf{x}) = \int_0^{T_{\max}} \mathbf{S}^S(\mathbf{x}, t) \cdot \mathbf{R}^S(\mathbf{x}, t) dt / \int_0^{T_{\max}} \mathbf{S}^S(\mathbf{x}, t) \cdot \mathbf{S}^S(\mathbf{x}, t) dt, \quad (12)$$

where the \cdot symbol denotes the scalar product (or dot product) of two vectors and $\mathbf{S}(\mathbf{x}, t)$ and $\mathbf{R}(\mathbf{x}, t)$ represent the source and receiver

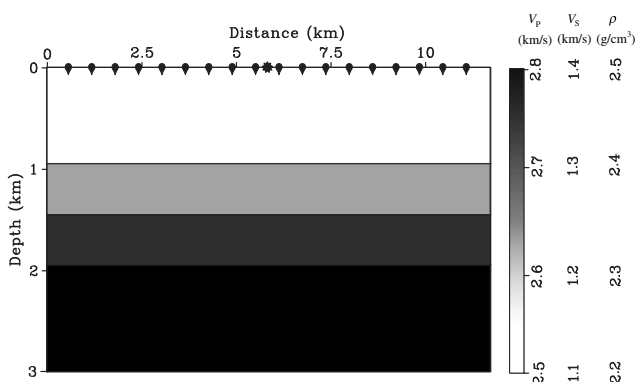


Figure 3. Flat three-reflector model: The star symbol represents a P-wave source, and the taper symbols represent receivers. The model contains 1150 points in the horizontal direction and 300 points in the vertical direction. We record the x - and z -particle velocities at all surface grid points as 2C synthetic seismic data for ERTM.

vector wavefields at propagation time t . The superscripts P and S denote the separated P- and S-wavefields, respectively, and \mathbf{x} is the location in the imaging space, I_{PP} , I_{PS} , I_{SP} , and I_{SS} are the PP, PS, SP, and SS mode migrated images, respectively. This imaging condition is for a single shot, and then a final stacked migrated image is produced by summing the images over all shots. Xiao and Leane (2010) and Shabelansky et al. (2015) take the similar idea of using scalar product to generate the PS image. Algebraically, dot product is the sum of the products of the corresponding components of two vector; geometrically, it is the product of the Euclidean magnitudes of the two vectors and the cosine of the angle between them. Note that the interpretation of these images is different from the conventional images produced by the scalar wavefield. If we only consider the numerators of equations 9–12, the images can be interpreted as the projection of the receiver vector wavefield onto the source vector wavefield. For example, the I_{PS} image is interpreted as the projection of the receiver vector S-wavefield onto the source vector P-wavefield. Normalization by source illumination makes the images more physical meaningful. The image amplitude does not represent the reflectivity, but it has a relatively correct dimensionless unit ($\text{amplitude}^2/\text{amplitude}^2$) and scale as the reflection coefficient. For large impedance contrasts and complex geologic structures, the imaging condition can also be improved by normalizing with the receiver illumination. Source normalization is an approximate, but practical and stable, way to do partial source illumination compensation, and it enhances the deeper reflectors (Kaelin and Guit-

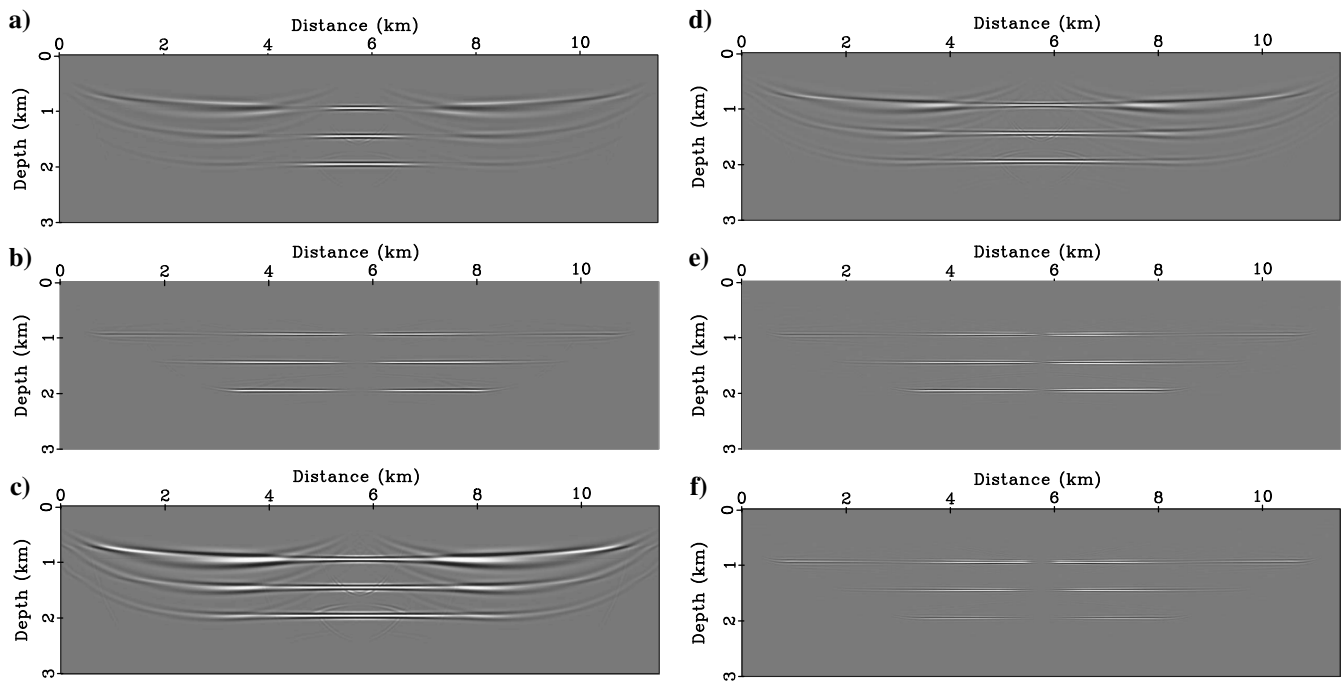


Figure 4. Single shot migration results: (a) PP and (b) PS images constructed by the proposed new imaging condition, (c) PP^r image from P-wave stress, (d) PP, and (e) PS images from the ERTM method based on Helmholtz decomposition, (f) PS image from Duan and Sava's (2015) cross-product imaging condition. Here, the amplitude and phase distortion caused by spatial derivative in Helmholtz decomposition are not corrected. The PP image in (a) from the dot-product imaging condition have a narrow imaging range. Like the analysis in Figure 1, the PP image amplitude is near zero at an approximately 45° incident angle when the reflector is flat. Compared with the PP images in (a and d), the PP^r images have a wider imaging range and better illumination. The amplitudes and phase are relatively accurate for critical and postcritical reflections. As for the PS images, both PS images in (b) from dot-product imaging condition and (f) from cross-product imaging condition have the consistent amplitude polarity, but the PS images in (b) have better illumination than the PS images in (f).

ton, 2006; Chattopadhyay and McMechan, 2008; Nguyen and McMechan, 2012).

Duan and Sava (2015) also present a scalar-product-based imaging condition to generate scalar images, in which geometric relationships, the reflector orientation, and the S-mode polarization direction are used to generate PS and SP images for pure wavefields obtained by Helmholtz decomposition. Even though both imaging conditions involve a dot product to produce the scalar field, they are very different. Based on the fact that P- and S-waves are orthogonal to each other, the basic principle to generate polarity-consistent converted-wave images in their method is to convert one mode's polarization direction onto another's by means of a cross product. As for the PS image, they first calculate the propagation direction (or polarization direction) of the P-mode, and then they rotate the P-mode propagation direction to the normal direction of the reflection plane, which is determined by the propagation direction of the P-wave and reflector's normal direction, by applying the cross product with the reflector's normal direction and then applying the dot product to the vector P- and S-modes to generate the scalar image. As for the SP image, they first convert the S-mode polarization direction into the reflection plane, and then they apply the dot product with

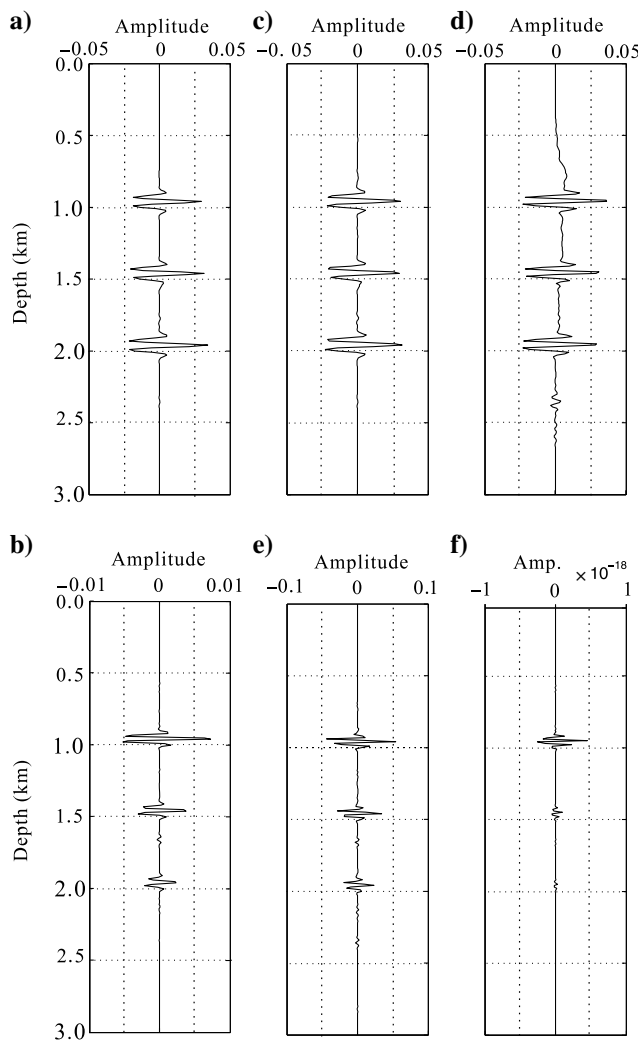


Figure 5. Traces at $x = 5.5$ km of images in Figure 4.

the reflector's normal vector to produce a scalar field, and finally they apply scalar multiplication to the scalar P- and S-modes to generate the scalar image. In our method, the basic principle to generate the polarity-consistent converted-wave images is to use the original pure mode vectors. In summary, in Duan and Sava's (2015) imaging condition, they convert one mode's polarity direction onto another's to generate polarity-consistent converted-wave images with the help of the reflector's normal direction, whereas using the dot-product-based imaging condition here avoids, rather than corrects, the polarity reversal. Moreover, in their approach, because few spatial derivatives are applied in the wavefield separation and imaging step, the amplitude and phase of the wavefields need to be corrected.

From the mathematic definition of the scalar product of two vectors that the sign of the scalar product depends on the sign of the cosine of the angle between these two vectors, the scalar-product-based imaging condition has the polarity reversal problem, too, but in the PP image. Figure 1 schematically shows the sign distributions of the PP and PS images as the offset changes: The black arrow line represents the forward time downgoing source P-wave wavefield, the blue arrow line represents the reverse time upgoing receiver P-wave wavefield, and the red arrow line represents the reverse time upgoing receiver S-wave wavefield. From the geometrical relationship of the source and receiver wavefields, the PP image amplitude from the scalar-product imaging condition implicitly contains a scaling factor $\cos(2\alpha)$ and the PS image amplitude contains $\sin(\alpha + \beta)$, where α is the P-wave incident (reflected) angle and β is the reflected S-wave angle. The reflection angle can be estimated from the half-aperture angle (Rosales et al., 2007). As the incident angle α increases, the sign of $\cos(2\alpha)$ varies from positive to negative, whereas $\sin(\alpha + \beta)$ keeps the same sign. This indicates that the sign of the PS-image is consistent as the offset increases, but the sign of PP-image changes at a certain offset, which depends on the dipping angle of the layer. Theoretically, when staking over dif-

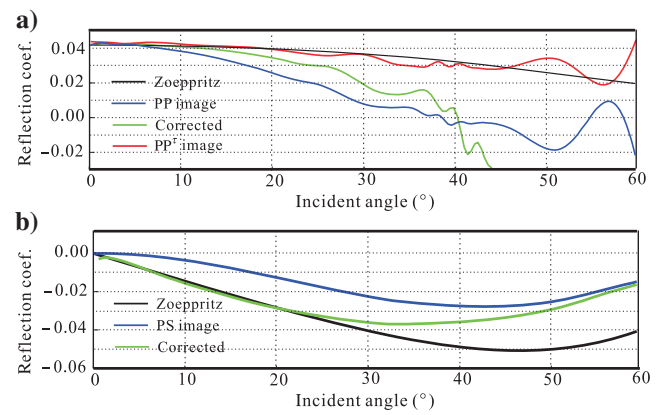


Figure 6. (a) PP and (b) PS reflection amplitudes for the first reflector. The blue curves are from scalar-product-based PP and PS images. The green curves are the corrected reflection amplitude using equation 13. The red curves are from the PP^r image. The black curves represent the corresponding reflection coefficient from solving the Zoepritz equation. The reflection amplitude directly from the source-normalized scalar-product-based imaging condition has the same dimensionless units, but it does not have the correct reflection amplitudes; whereas the corrected results perform better, the amplitudes follow the analytical reflection coefficients up to approximately 30° . The PP^r image behaves best in comparison; it closely follows the analytical reflection coefficient up to approximately 45° .

ferent shots, such a polarity change may also destroy the events, especially in the shallow region. Fortunately, in practice, this problem can be easily avoided by muting the large angle reflections in common angle-image gathers or just applying a mute in the common-shot domain.

Compared with the source-normalized crosscorrelation condition for scalar fields, the image amplitude from the scalar-product imaging condition is smaller than the true reflection amplitudes. Thus, if angle-dependent reflectivity is needed, we suggest compensating the image amplitude in the angle domain; for example, the relatively amplitude-preserved PP image $I'_{\text{PP}}(\mathbf{x}, \theta)$ can be generated by

$$I'_{\text{PP}}(\mathbf{x}, \theta) = I_{\text{PP}}(\mathbf{x}) / (\cos(\theta) + \varepsilon^2), \quad (13)$$

where θ is the angle between the incident and reflected P-waves. A small number ε^2 should be added to the denominator to prevent division by zero. The propagation directions of the incident and reflected P- and S-waves can be calculated from the P- and S-wave Poynting vectors.

P-wave stress image

Besides the pure vectors, the decoupled wave equation generates another pure wave mode, P-wave stress. The introduction of auxiliary P-wave stress wavefields presents the possibility to generate a better migration scalar image. Not like the method that Wang and McMechan (2015) discuss, we simply perform the conventional crosscorrelation (Claerbout, 1971) imaging conditions onto the P-wave stress wavefields, rather than the magnitude, to generate the P-wave stress image (to differentiate from the PP image from the scalar product, here we call P-wave stress image the PP^r image). Here, the source-normalized zero-lag crosscorrelation imaging condition

$$I_{\text{PP}^r}(\mathbf{x}) = \int_0^{T_{\max}} \tau_S^P(\mathbf{x}, t) \tau_R^P(\mathbf{x}, t) dt / \int_0^{T_{\max}} \tau_S^P(\mathbf{x}, t) \tau_S^P(\mathbf{x}, t) dt \quad (14)$$

is used to produce the PP^r image, where τ_S^P and τ_R^P represent the source and receiver P-wave stress wavefields, respectively. The deconvolution (Valenciano and Biondi, 2003) imaging condition is also easily used to obtain an amplitude-friendly PP^r result. Theo-

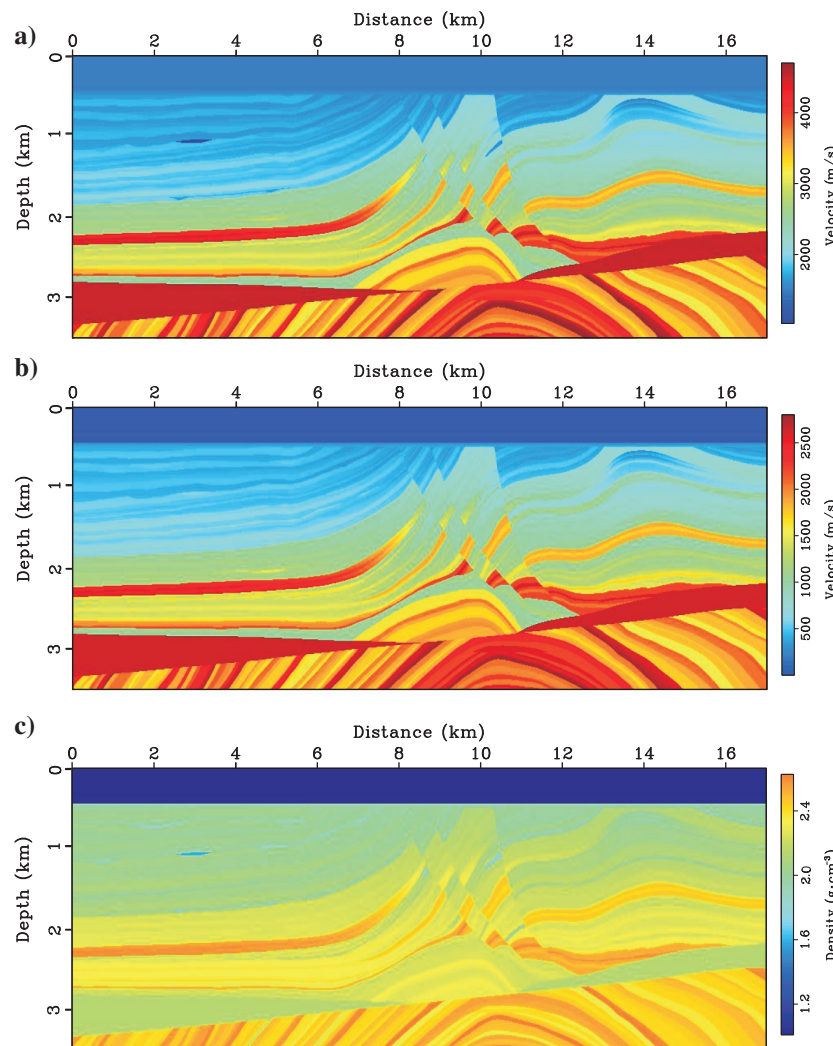


Figure 7. Elastic Marmousi2 model: (a) P-wave velocity, (b) S-wave velocity, and (c) density.

retically, we produce five scalar images (PP, PS, SP, SS, and PP^r) simultaneously. Although the analysis is restricted to the 3C seismic data, the introduction of pure stress wavefields makes it possible to image marine 4C seismic data jointly by injecting the pressure data into the auxiliary P-wave stress wavefield and the vector 3C data into the elastic wave equation.

From the discussion about decoupled wave equation, the time derivative of the τ^P wavefield ($d\tau^P/dt$) is actually equal to the divergence of the particle-velocity wavefield if we ignore the scaling factor $b(\lambda + 2\mu)$. So it is also possible to generate the scalar PP^r image using $d\tau^P/dt$. But we hold the idea that the τ^P wavefield is more suitable for the PP^r image due to its meaningful physical interpretation. It is reasonable to treat the PP^r image as a replacement of the PP image generated from the scalar-product imaging condition to avoid the polarity change. But to avoid confusion, in this paper, we treat the PP^r image as a by-product of 3C seismic data elastic RTM.

As for the S-wave, unfortunately, we have not found a single variable τ^S that can represent the S-wave stress. The τ^S wavefield can be constructed through $\tau_{ij}^S = \tau_{ij} - \delta_{ij}\tau^P$ (Xiao and Leaney, 2010) or $\dot{\tau}_{ij}^S = \dot{\tau}_{ij} - \delta_{ij}\tau^P$ (Li et al., 2007). In Appendix B, we adopt the second method. Unlike P-wave stress, S-wave stress is a 3×3 tensor and, moreover, S-wave stress contains P-wave energy. To remove the strong P-wave energy, another S-wave stress tensor

is constructed by using “acoustic” S-wave equation B-2 to transform the S-wave particle-velocity to the S-wave stress tensor (to differentiate it from τ^S , we call it the S-wave quasi-stress tensor τ^{qS}). From the discussion in Appendix B, we can use this S-wave quasi-stress tensor τ^{qS} to generate polarity-consistent converted-wave images (PS, SP, and SS) for geologic structures. However, in 3D case, the approach of crosscorrelating pure stress generates nonunique converted-wave images.

NUMERICAL EXAMPLES

In this section, we illustrate our method using several synthetic models: 2D and 3D layered models, resampled Marmousi2 model, and 3D SEG/EAGE salt model. Figure 2 shows a flow chart of ERTM based on the scalar imaging condition with vector P- and S-wave wavefields and the auxiliary P-wave stress wavefields. The snapshots of the source wavefield can be calculated and saved before receiver wavefield construction or reconstructed from information generated during forward source wavefield extrapolation (Nguyen and McMechan, 2009). Here, we save the source wavefield in 2D tests and reconstruct the source wavefield using the boundary values in 3D tests. In these numerical examples, elastic multicomponent data are generated by using an eighth order in space, second order in time, staggered-grid finite-difference

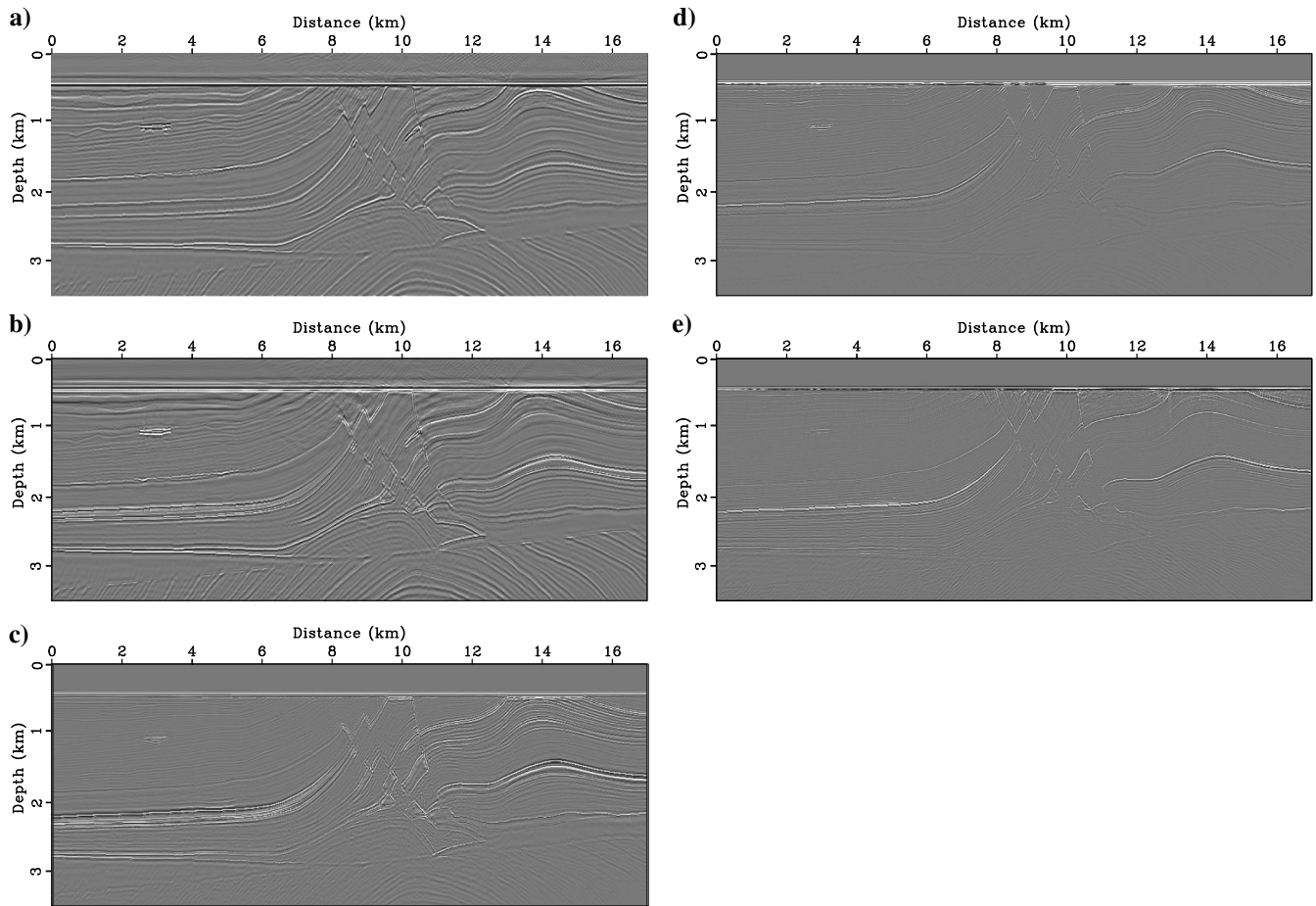


Figure 8. Migration results of Marmousi2: (a) PP^r, (b) PP, (c) PS, (d) SP, and (e) SS images. Not only the flat and dipping layers, but also the three faults and the two anticlines are imaged clearly and correctly.

scheme. The parallel algorithm based on GPU acceleration is used to speed up the calculation. We use a 20-grid perfectly matched layer (Collino and Tsogka, 2001) boundary condition to suppress the artificial boundary reflections. The sources for all tests are explosive Ricker wavelets with a 30 Hz dominant frequency. The crosscorrelation imaging condition creates strong low-wavenumber migration artifacts generated by the crosscorrelation of reflections, back-scattered waves, head waves, and diving waves. A Laplacian filter (Youn and Zhou, 2001) is then applied to suppress low-wavenumber artifacts. For the spectrum and amplitude compensation, the seismic data are integrated twice to correct the spectrum distortion and rescale the migration output by a factor $V_p^2/4$ for PP and PP^r images, $V_p V_s/4$ for PS and SP images, and $V_s^2/4$ for an SS image; here, V_p, V_s are the P- and S-wave velocities.

2D flat-layered model

Consider a 2D flat three-layered model with 10 m grid spacing in the x - and z -directions as shown in Figure 3. To examine the

migration accuracy at a large offset, the model contains 1150 points in the horizontal direction and 300 points in the vertical direction. We record the x - and z -particle velocities at all surface grid points as 2C synthetic seismic data. The time sample increment is 1.0 ms. A P-wave source is located at point (5.75 and 0 km). Migration results from using slightly smoothed velocities and density by a nine-point, weighted-average smooth filter are shown in Figure 4: (a) PP and (b) PS images constructed by the proposed VB-ERTM method, (c) PP^r image from P-wave stress, (d) PP and (e) PS images from ERTM method based on Helmholtz decomposition, and (f) PS image from Duan and Sava's (2015) "cross-product" imaging condition. Figure 5 presents the traces at $x = 5.5$ km of images in Figure 4. From Figures 4 and 5, we see that the PP image in (a) from the scalar-product-based imaging condition has a narrow imaging range. As the analysis in Figure 1, the PP image amplitude is near zero at an approximately 45° incident angle if the reflector is flat. The critical angle for the first reflector is approximately 74.0°. With further offset increases after 45°, strong, low-wavenumber noise contaminates the effective reflectors' information. We hardly see

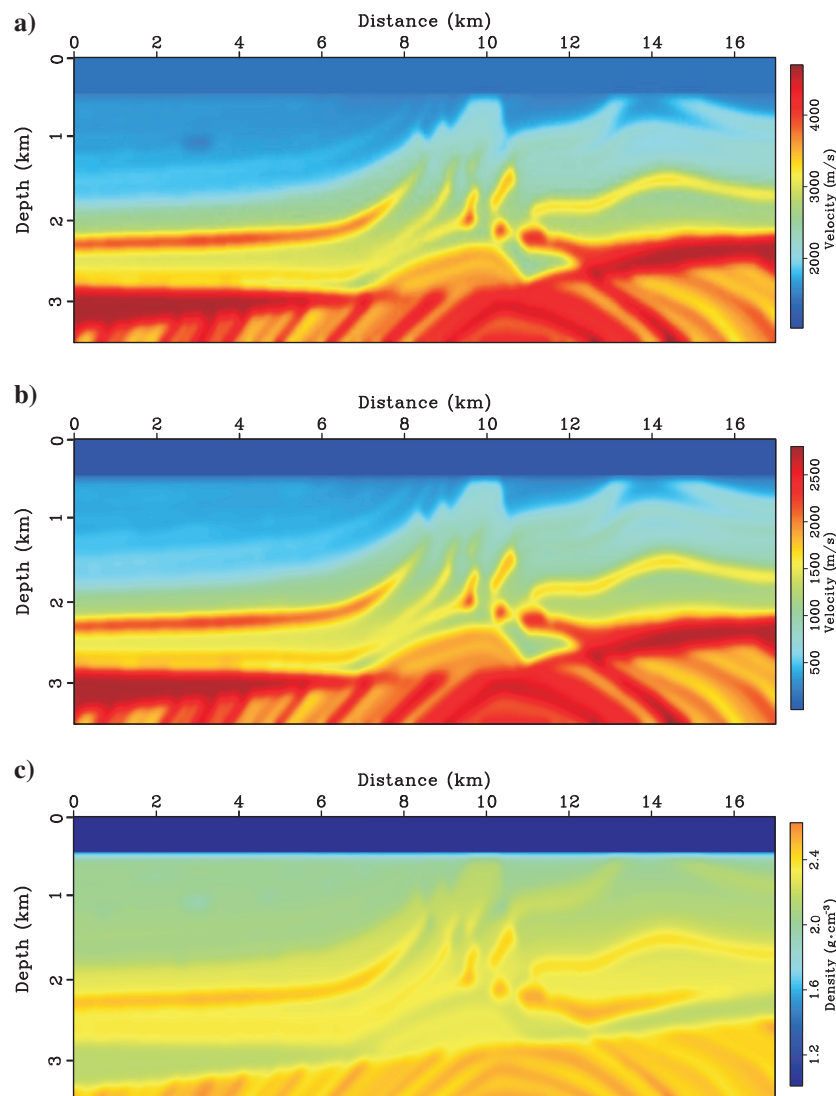


Figure 9. Smoothed elastic Marmousi2 model: (a) P-wave velocity, (b) S-wave velocity, and (c) density.

the polarity changes in the PP image. Compared with the PP image in (a), the PP^r images have a wider imaging range and better illumination. Amplitudes and phase are relatively accurate for critical and postcritical reflections. As for PS images, PS images in (b) from “dot-product” imaging condition and (f) from the cross-product imaging condition have consistent amplitude polarity, not like the PS image in (e), but PS images in (b) have better illumination than PS images in (f).

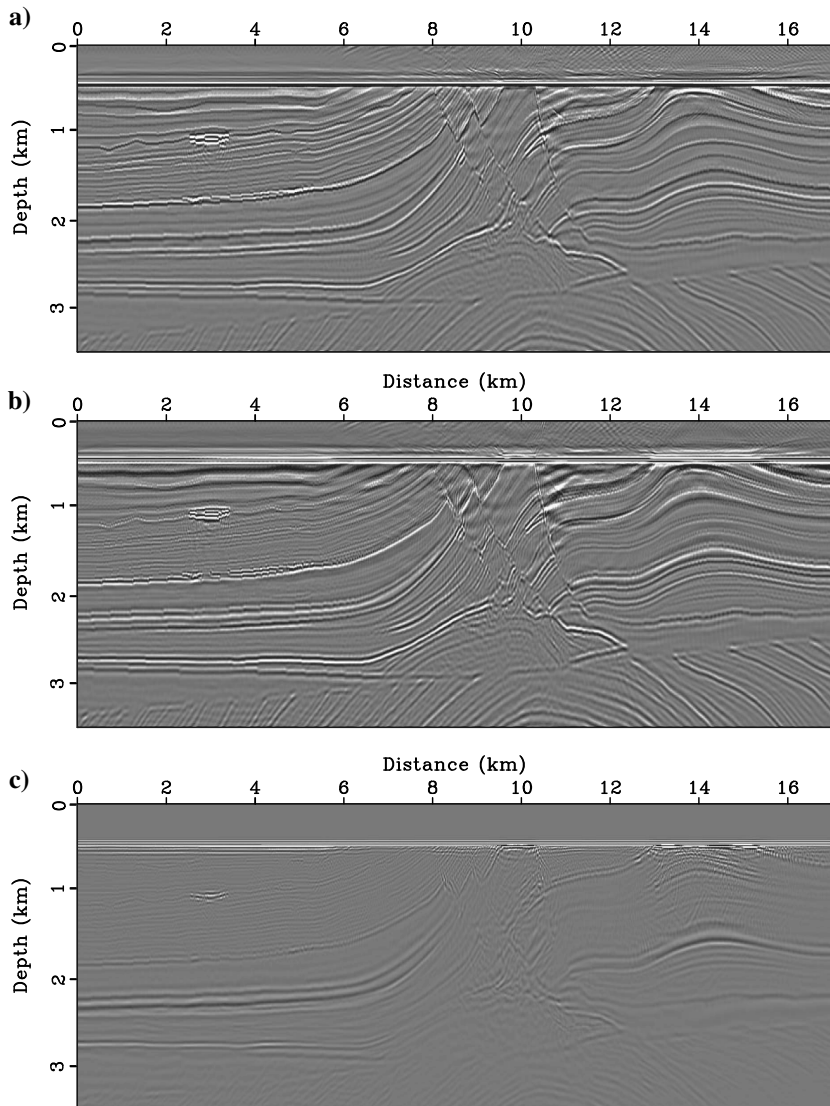
Figure 6 shows image amplitudes (blue curves for PP and PS images and red curves for PP^r image) from the first reflector in Figure 4a–4c, the corresponding analytical reflection coefficients (black curves) from solving the Zoeppritz equation, and the corrected image amplitudes (green curves) by using equation 13. We use a small window in depth around the first reflector to extract the maximum amplitude from each trace in the migrated images. From Figure 6, we see that the image amplitudes directly extracted from the images are smaller than the analytical reflection coefficients, but they have correct dimensionless units and the same scale as the analytical reflection coefficients. The corrected amplitudes

match better; they closely follow the analytical reflection coefficients up to approximately 30° . However, as the incident angle increases, errors between the corrected and analytic curves become large. The PP^r image behaves best in comparison; it closely follows the analytical reflection coefficient up to approximately 45° . On the whole, the source-normalized scalar-product-based imaging condition provides a more accurate PS image than the PP image; on the other hand, the PP^r image from P-wave stress is more reliable. In practice, it is reasonable to treat the PP^r image as the final PP image for subsequent interpretation due to its wide imaging range and reliable angle-dependent reflection amplitude.

Marmousi2 model

Here, a resampled Marmousi2 model (Martin et al., 2006), shown in Figure 7, is used to further show the feasibility and validity of the proposed method in the aspects of imaging capability of complex structures. The resampled model contains 1700 points in the horizontal direction and 350 points in the vertical direction. A total of

Figure 10. Migration results of the Marmousi2 model with inaccurate models: (a) PP^r , (b) PP, and (c) PS stacked images



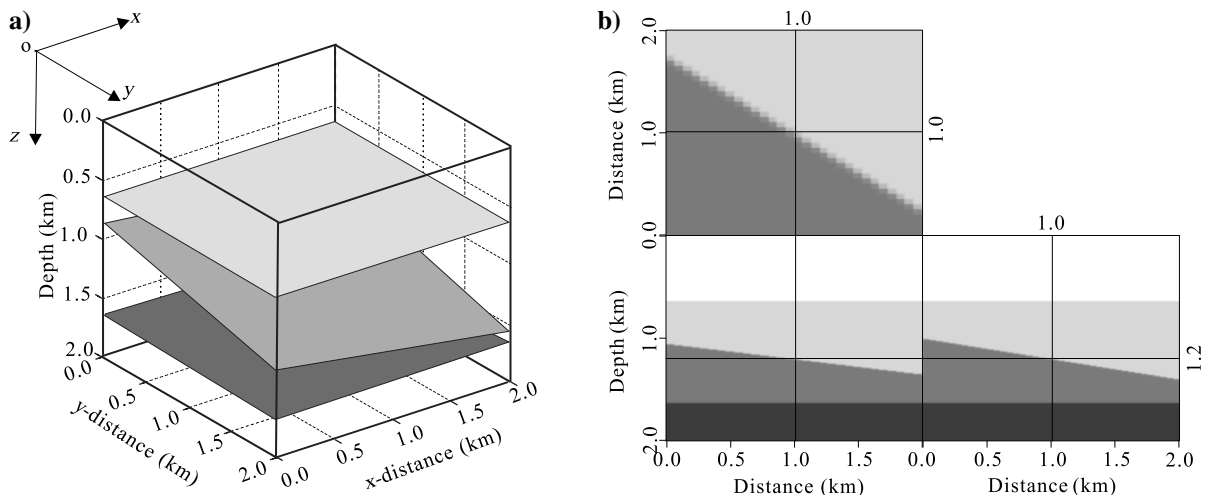


Figure 11. (a) 3D coordinate system and 3D elastic model. (b) Profiles on the vertical slice along line $z = 1.2$, $x = 1.0$, and $y = 1.0$ km. The P-wave velocity V_P from the top layer is 2.5, 3.0, 3.5, and 4.0 km/s, the S-wave velocity is defined as $V_S = V_P/1.73$, and the density model follows Gardner's relation: $\rho = 0.23V_P^{0.25}$.

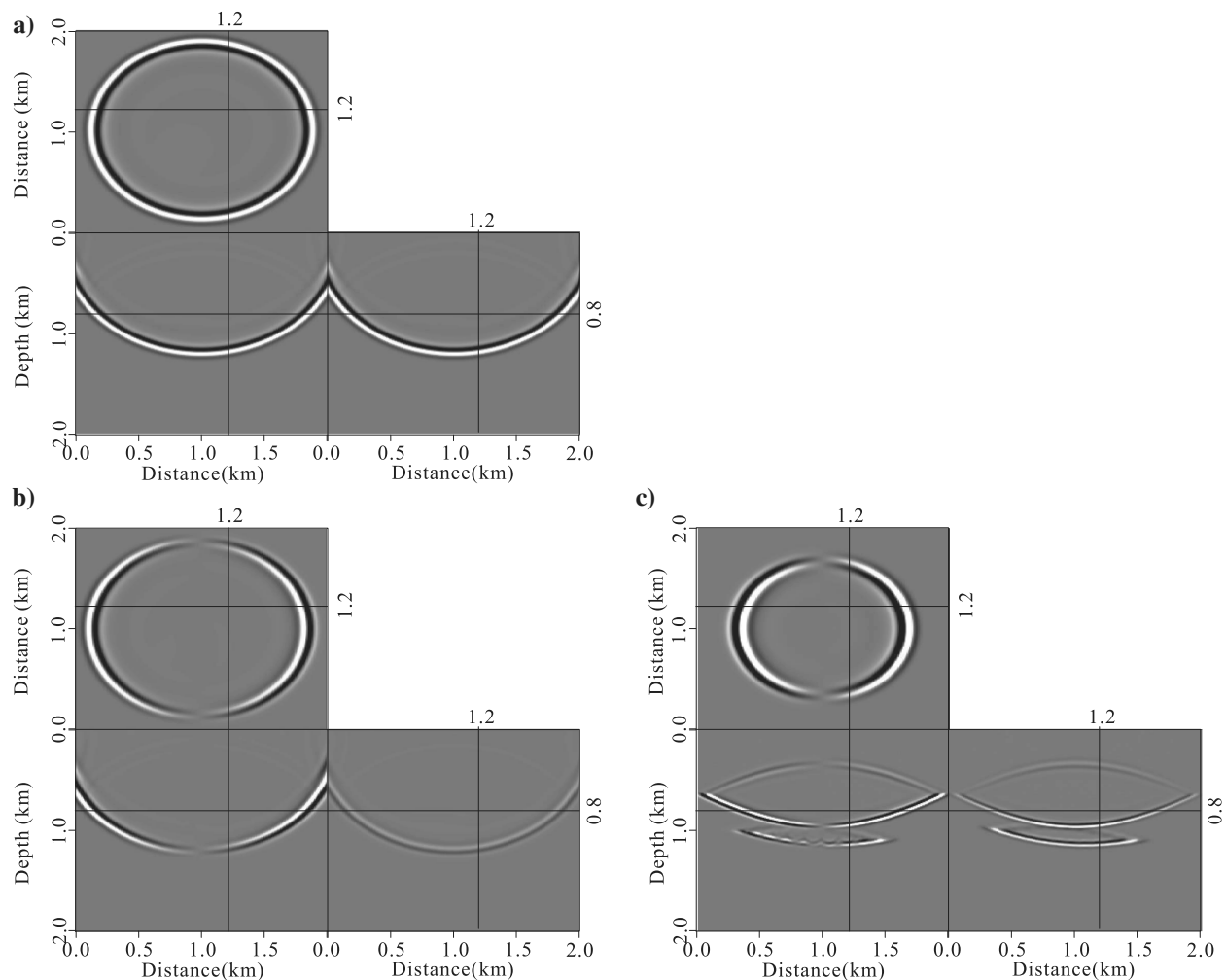


Figure 12. Separated wavefield snapshots at 0.25 s: (a) P-wave stress, (b) x -component of P-wave particle velocity, and (c) x -component of S-wave particle velocity.

170 shots were simulated with a source interval of 100 m starting from the left edge of the model. All of the sources are at a water depth of 10 m, and receivers are located near the seafloor. The spread length of the receiver is 3.2 km, with a distance of 10 m. The space step is 10 m in the x - and z -directions, the time step is 1.0 ms, and the total record time is 5 s.

Figure 8 shows the migration results. The PP and PP^r images exhibit structurally equivalent results, the images are very clear, and the events are well-focused. Not only the flat and dipping layers, but also the three faults, unconformity, and the two anticlines, are all imaged clearly and correctly. The events of the PP and PP^r images are consistent and are all imaged at the same depth. In the PS image, we can see that the main structures are well-imaged. However, the shallow flat layers are not clear because the PP and PP^r images due to the low S-wave velocity contrast, from the seafloor to underground $z = 1.5$ km depth S-wave velocity, vary

approximately from 0 to 600 m/s. For the SP and SS images, similar conclusions can be obtained. Only an explosive source is used: The energy of converted waves in the source wavefield is weak, so the SP and SS images are not as clear as the PP, PS, and PP^r images.

Furthermore, heavily smoothed, inaccurate velocity models (as shown in Figure 9) are used to evaluate the robustness of the proposed method. The smoothed models are obtained by applying a nine-point, weighted-average smooth filter 100 times. Velocity models used for RTM are usually assumed to be sufficiently smooth to suppress artifacts generated by secondary reflections or backscattered events during source or receiver extrapolations (Nguyen and McMechan, 2015). Here, only the migrated PP^r , PP, and PS images are considered. Figure 10 shows the migration results from using inaccurate migration velocity models. We see that the PS image is more sensitive to the migration velocity than the PP and PP^r images. The accuracy of the PS image decreases, the events near the

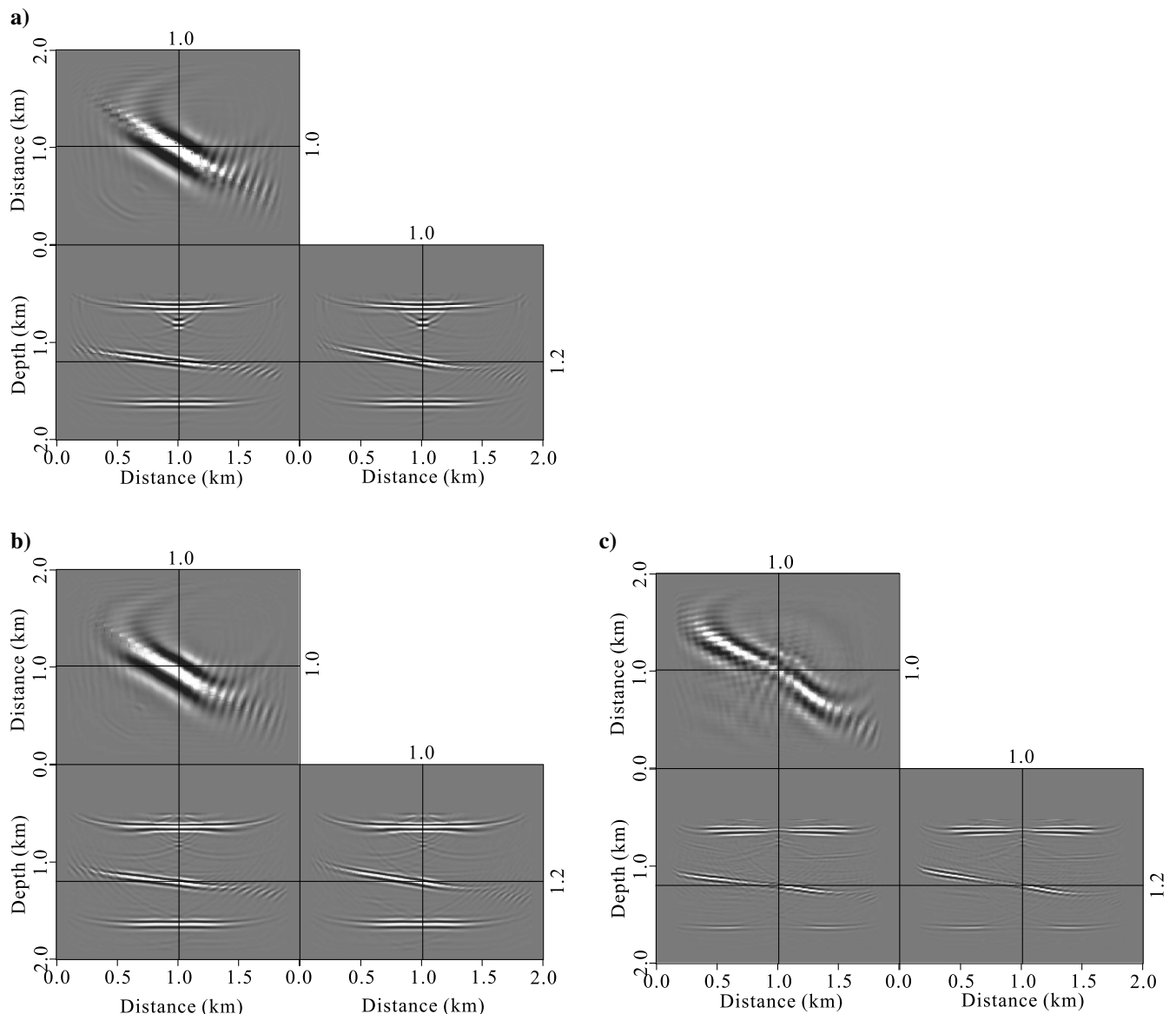


Figure 13. Single-shot (a) PP^r , (b) PP, and (c) PS images of the layered model using the proposed imaging conditions.

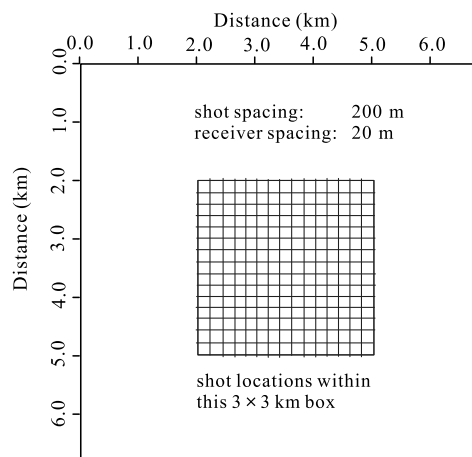


Figure 14. Geometry of the elastic simulation receiver area and shot patch.

upper anticline, and the unconformity plane become blurred and discontinuous; the gas-charged sand channel is also inaccurately evaluated. But the profile of the main subsurface structures is still well-exhibited. Compared with the PS image, the PP^r and PP images are much less affected.

Simple 3D layered model

A simple layered model is used to verify the effectiveness of the proposed method in a 3D application. As shown in Figure 11, the model contains two flat reflectors and one dipping reflector in middle. The spatial sampling step is 10 m in all directions. A P-wave source is located at grid coordinate (1.0, 1.0, and 0 km), and receivers at all grids record particle-velocity multicomponent data. We reconstruct, rather than save, source wavefields from using boundary values saved during the forward source wavefield extrapolation to reduce the excessive storage requirement (Nguyen and McMechan, 2009). Figure 12 shows snapshots of the P-wave

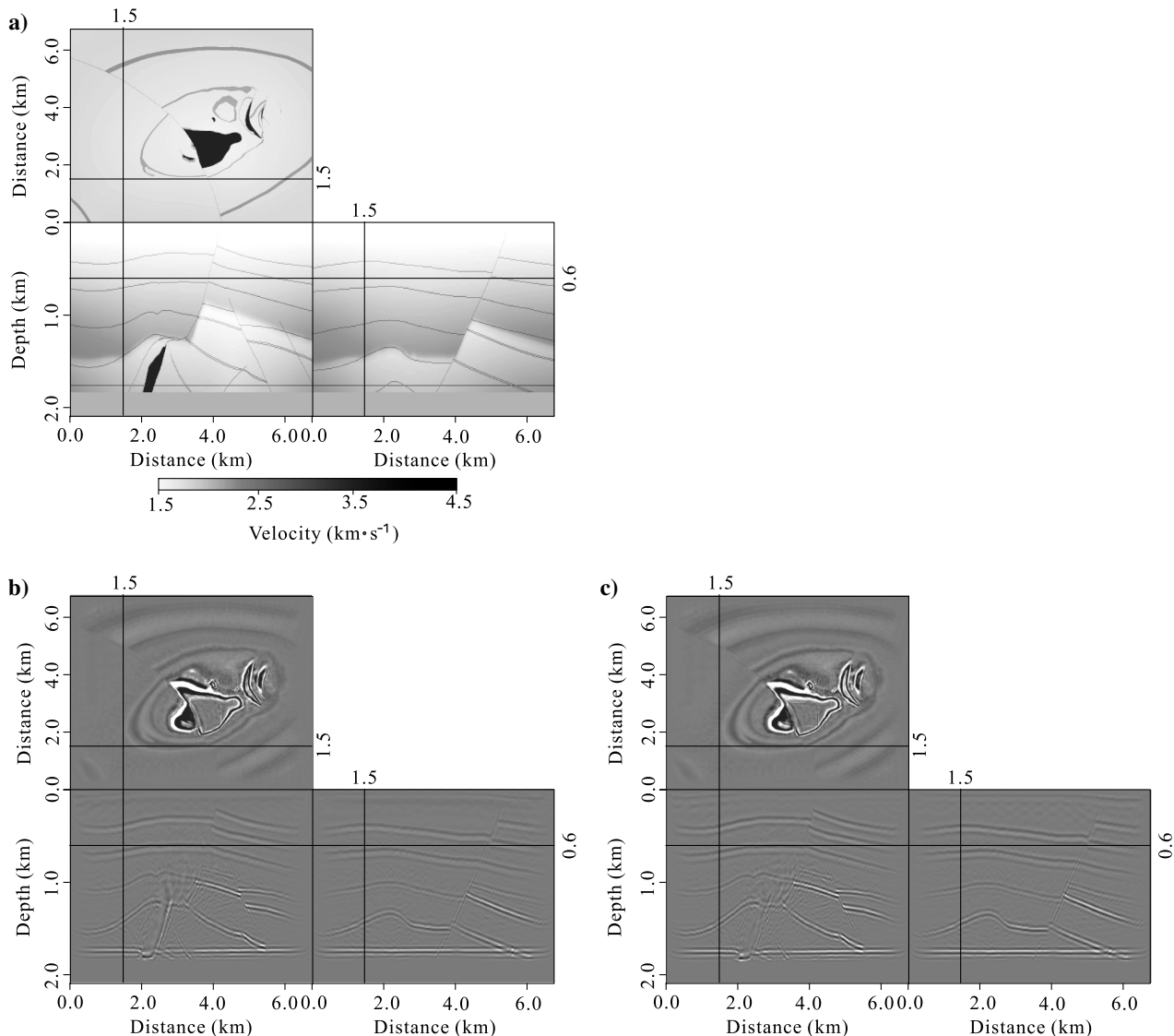


Figure 15. 3D ERTM images of (a) SEG/EAGE salt data at $x = 1.5$, $y = 1.5$, and $z = 0.6$ km; (b) PP and (c) PS images.

stress and x -components of P- and S-wave particle velocities at 0.25 s. We see that the decoupled P- and S-wave equations provide satisfactory separation results for 3D VB-ERTM. The migrated PP^r , PP, and PS images are shown in Figure 13. We see that the PP^r , PP, and PS images have correctly mapped the reflectors and keep a consistent polarity within a reliable aperture, which shows that the scalar imaging condition works for the 3D case.

3D SEG/EAGE salt model

The 3D SEG/EAGE salt model has a complicated structural nature, which is representative of salt intrusions in the Gulf of Mexico (Yoon et al., 2003). It is a challenging standardized test for 3D prestack depth-migration algorithms. Its elastic version, modified from the acoustic version by setting S-wave velocity $V_S = V_P/1.73$ and $\rho = 0.23V_P^{0.25}$, to test the validity of our proposed method in 3D

application with complicated geologic structures. The model contains $676 \times 676 \times 210$ grid points, which correspond to 6.76 km inline, 6.76 km crossline, and 2.1 km depth. There are 256 shots within a 3×3 km box at the surface of the model (Figure 14) to generate the 3D-3C multicomponent seismic data. The receivers are fixed at the surface of the model with a 20 m spatial interval to record the particle-velocity wavefield. The record length is 4 s. We carried out ERTM tests with smoothed models. Figures 15 and 16 show the migration results of the 3D SEG/EAGE salt model; each includes the stacked PP and PS images. Figure 15 shows the data volumes with three slices at $x = 1.5$, $y = 1.5$, and $z = 0.6$ km, mainly containing several dip reflectors and a small part of the salt. Figure 16 shows the data volumes with three slices at $x = 3.0$, $y = 3.0$, and $z = 1.0$ km, which are just crossing the salt body. We see that our ERTM algorithm gives a clear, correct view of the salt body. The images suffer no polarity reversal and so the stacked events are consistent.

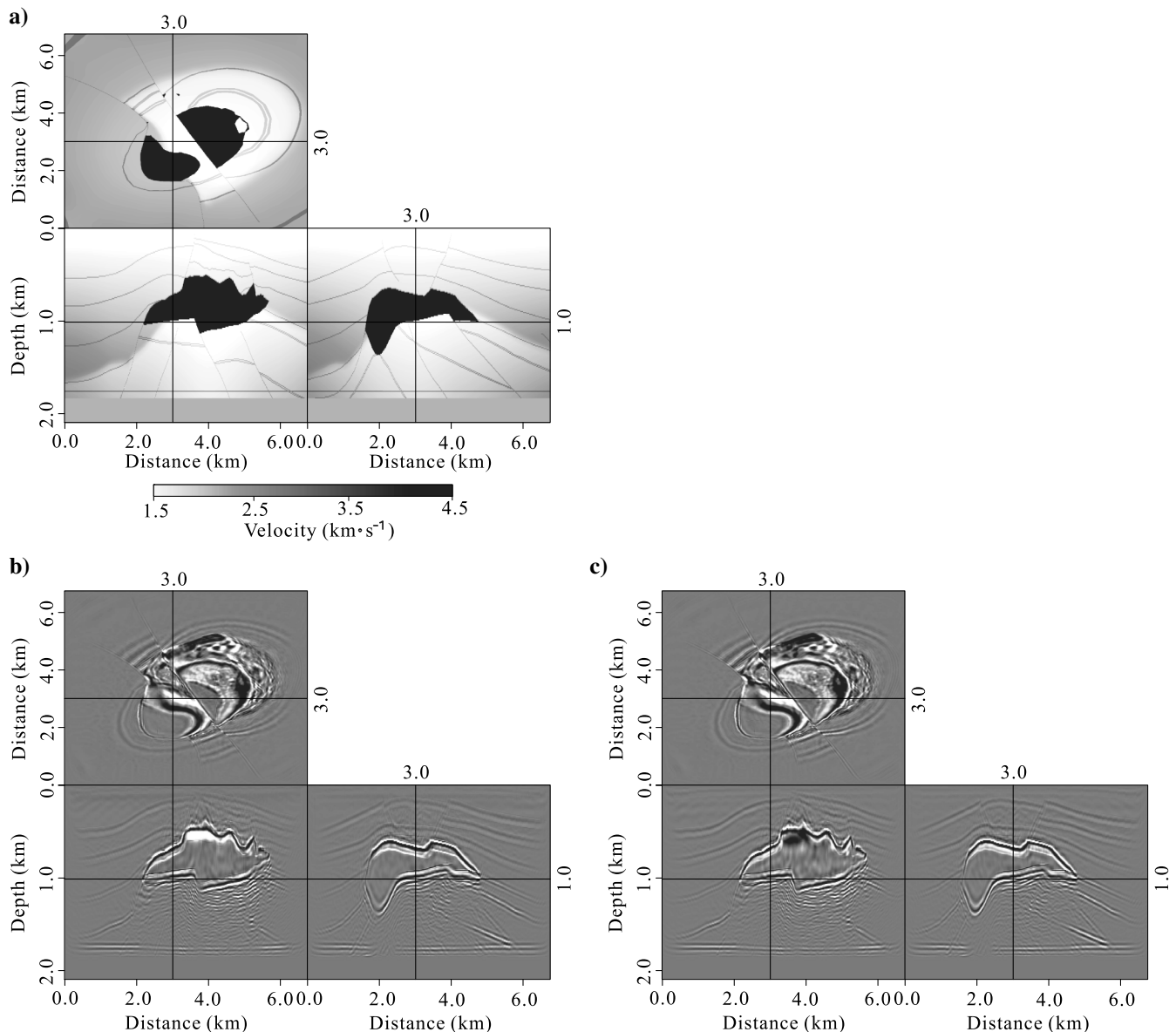


Figure 16. 3D ERTM images of (a) SEG/EAGE salt data at $x = 3.0$, $y = 3.0$, and $z = 1.0$ km: (b) PP and (c) PS images.

CONCLUSION

We have presented a stable and simple ERTM method for multicomponent seismic data. The method is based on the decoupled wave equation to separate wavefields. Instead of crosscorrelating the Cartesian components between two vector wavefields, the scalar product of two vector wavefields with source-normalized illumination is exploited to produce the scalar images. Compared with the various coordinate-dependent images, each scalar image has a unique geophysical interpretation whether in the 2D or 3D case. The proposed ERTM for multicomponent elastic data is also different from the method based on Helmholtz decomposition wavefield separation. Our method needs no polarity reversal corrections for converted-wave images or additional amplitude and phase corrections for pure wave modes. The polarity change in PP-images can be easily avoided by muting the large angle reflections in the angle domain or the large offset reflections in the shot domain. It is also feasible to use the PP^r image from crosscorrelating P-wave stress as the final PP image to avoid such polarity change. Numerical examples on simple 2D and 3D flat models, Marmousi2, and 3D SEG/EAGE salt model demonstrate that the proposed imaging condition can provide relatively accurate images. The possibility of converted-wave images using the S-wave stress tensor is also discussed. The proposed S-wave quasi-tensor provides a promising solution for converted-wave images in ERTM. However, there are many aspects needing further investigations. The method currently is not recommended for application in anisotropic media because the current decoupled wave equation cannot separate two shear (SH and SV) waves and S-wave splitting may make the situation more complicated.

ACKNOWLEDGMENTS

We greatly appreciate the support of the National Science Foundation of China (41574125), Large-scale Oil & Gas Field and Coalbed Methane Development Major Projects (2016ZX05018-005), Research of the China National Petroleum Corporation (2016A-3302), and Fundamental Research Funds for Central Universities (15CX08002A). We thank M. Zhang, D. Han, and X. Zhang for their helpful suggestions. We also acknowledge J. Shragge, F. Liu, and the anonymous reviewers for reviewing this manuscript and their constructive suggestions and comments to the revision that have greatly improved this manuscript.

APPENDIX A

THE NONCONVERSION CONDITION FOR DECOUPLED P- AND S-WAVE EQUATIONS

In this section, we theoretically prove that the decoupled wave equation cannot separate the wavefield completely. A related investigation on this topic has been discussed in Yao (1996). Yao (1996) points out that conversion does not occur if and only if $\nabla\rho = \nabla\mu = 0$. The analysis starts from the displacement equation as follows for

infinitesimal motion in an elastic isotropic medium (Kelly et al., 1976; Yao, 1996):

$$\begin{aligned} \rho\ddot{\mathbf{u}} &= (\lambda + 2\mu)\nabla(\nabla \cdot \mathbf{u}) + \nabla\lambda(\nabla \cdot \mathbf{u}) - \mu\nabla \times (\nabla \times \mathbf{u}) \\ &\quad + \nabla\mu \times (\nabla \times \mathbf{u}) + 2(\nabla\mu \cdot \nabla)\mathbf{u}, \end{aligned} \quad (\text{A-1})$$

where \mathbf{u} is the displacement wavefield, ρ is the density, and λ and μ are the Lamé parameters. Applying divergence to both side of equation A-1 and letting $\nabla \cdot \mathbf{u} = \theta$ (represents P-wave) and $\nabla \times \mathbf{u} = \mathbf{s}$ (represents S-wave) yields

$$\begin{aligned} \nabla\rho \cdot \ddot{\mathbf{u}} + \rho\ddot{\theta} &= (\lambda + \mu)\nabla^2\theta + \nabla(\lambda + \mu) \cdot \nabla\theta + \nabla\mu \cdot \nabla^2\mathbf{u} \\ &\quad + \mu\nabla^2\theta + \nabla\theta \cdot \nabla\lambda + \theta\nabla^2\lambda + \mathbf{s} \cdot (\nabla \times \nabla\mu) \\ &\quad - \nabla\mu \cdot (\nabla \times \mathbf{s}) + 2\nabla(\nabla\mu \cdot \nabla) \cdot \mathbf{u} \\ &\quad + 2(\nabla\mu \cdot \nabla)\nabla\theta. \end{aligned} \quad (\text{A-2})$$

Considering $\mathbf{u} = \mathbf{u}^P + \mathbf{u}^S$, equation A-2 indicates that S-wave terms containing \mathbf{s} or \mathbf{u}^S vanish if $\nabla\rho = \nabla\mu = 0$; i.e., the P-wave equation characterizing the P-wave propagation can be separated from the heterogeneous elastic wave equation if and only if $\nabla\rho = \nabla\mu = 0$. For the S-wave displacement, we can obtain a similar conclusion by applying the curl operator to equation A-1. Yao (1996) refers $\nabla\rho = \nabla\mu = 0$ as the nonconversion condition. This condition guarantees that energy cannot converts at interfaces.

Now, we evaluate the accuracy of a decoupled wave equation by an inhomogeneous model with the horizontal and vertical sharp interfaces shown in Figure A-1a. Here, only S-wave results are shown. Figure A-1b shows the x-component of decoupled S-wave particle velocity. In Figure A-1b, we see abnormal energy along the interface. Fortunately, the abnormal energy is distributed within a very narrow area along the interface, maybe just at one or two

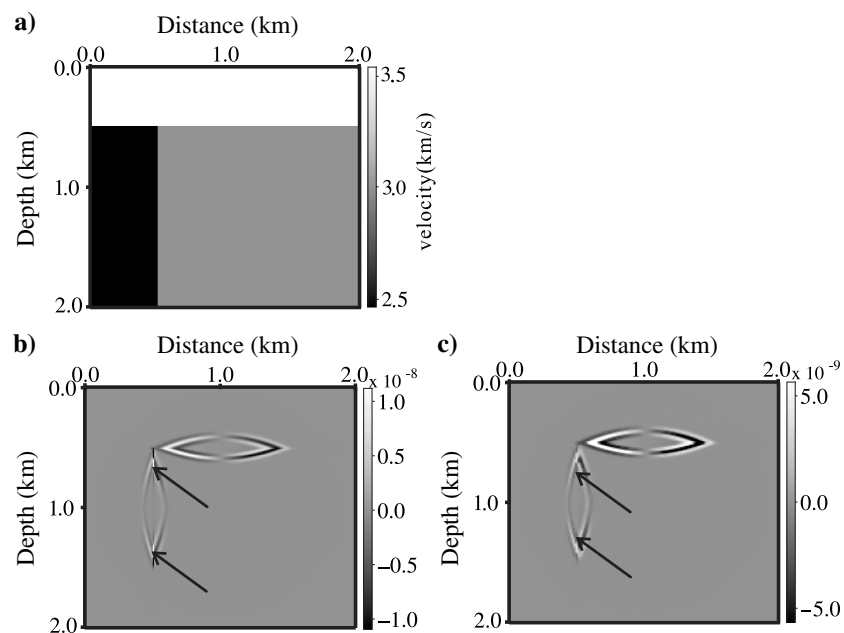


Figure A-1. Inhomogeneous model (a) with horizontal and vertical sharp interfaces and the x-component of (b) decoupled S-wave and (c) the one after median filtering.

nodes. So we can remove or weaken the abnormal energy through smooth or median filtering. Figure A-1c shows the decoupled S-wave after simple median filtering. Most of the abnormal energy is removed. For decoupled P-wave wavefield, similar conclusions can be obtained. Also, we can avoid (or alleviate) such a problem by using the smooth models. Basically, decoupled P- and S-wave equations can provide satisfactory separation results for VB ERTM.

APPENDIX B EQUIVALENT DECOUPLED P- AND S-WAVE EQUATIONS

From equation 7, we can alternatively obtain a 2D stress-particle velocity equation as follows (Li et al., 2007):

$$\begin{aligned} \text{Total wavefields: } & \begin{cases} v_x = v_x^P + v_x^S, \\ v_z = v_z^P + v_z^S, \end{cases} \\ \text{P-wave part: } & \begin{cases} \dot{v}_x^P = (\lambda + 2\mu)(v_{x,x} + v_{z,z}), \\ \dot{v}_x^P = b\tau_{xx}^P, \\ \dot{v}_z^P = b\tau_{zz}^P, \end{cases} \\ \text{S-wave part: } & \begin{cases} \dot{v}_{xx}^S = -2\mu v_{z,z}, \\ \dot{v}_{zz}^S = -2\mu v_{x,x}, \\ \dot{v}_{xz}^S = \mu(v_{x,z} + v_{z,x}), \\ \dot{v}_x^S = b(\tau_{xx,x}^S + \tau_{xz,x}^S), \\ \dot{v}_z^S = b(\tau_{xz,x}^S + \tau_{zz,x}^S). \end{cases} \end{aligned} \quad (\text{B-1})$$

From equation B-1, we see that the S-wave stress wavefield τ^S is not one single variable but a tensor, and it consists of three components

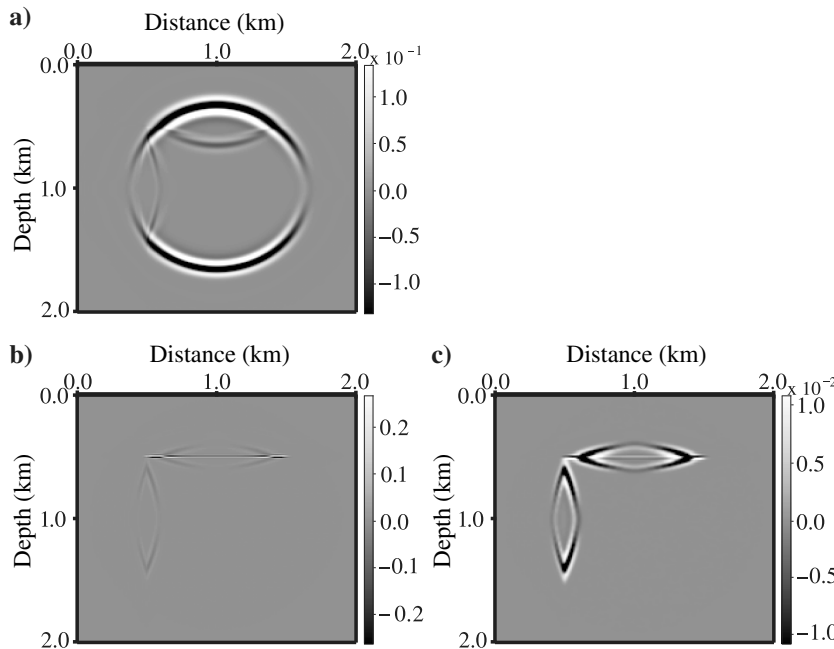


Figure B-1. (a) The τ_{xx}^S of S-wave stress tensor, (b) τ_{xx}^{QS} of the S-wave quasi-stress tensor, and (c) τ_{xx}^{QS} of the S-wave quasi-stress tensor after smooth and median filtering. It is clear that the S-wave stress contains strong P-wave energy, whereas the S-wave quasi-stress tensor does not contain it, so strong P-wave energy and the abnormal energy are removed significantly after smooth and median filtering.

$(\tau_{xx}^S, \tau_{zz}^S, \tau_{xz}^S)$ in the 2D case (six in the 3D case). Moreover, the S-wave stress actually contains strong P-wave energy, as shown in Figure B-1a. This means that the S-wave stress cannot represent the pure S-wave mode.

Actually, it is feasible to use the acoustic S-wave equation (the third part of equation B-1) to transform the decoupled S-wave particle-velocity wavefield to the S-wave stress wavefield. The 2D acoustic S-wave equation can be expressed as

$$\begin{cases} \dot{\tau}_{xx}^{QS} = -2\mu v_{z,z}^S, \\ \dot{\tau}_{zz}^{QS} = -2\mu v_{x,x}^S, \\ \dot{\tau}_{xz}^{QS} = \mu(v_{x,z}^S + v_{z,x}^S), \end{cases} \quad (\text{B-2})$$

where $\tau^{QS} = (\tau_{xx}^{QS}, \tau_{zz}^{QS}, \tau_{xz}^{QS})$ represents the S-wave stress tensor because it is different than the τ^S wavefield, we refer it as the S-wave quasi-stress tensor. From equation B-2, we know $\tau_{xx}^{QS} = -\tau_{zz}^{QS}$ if the abnormal energy along the interfaces is weak or can be suppressed to negligible extent. However, the numerical results in Figure B-1b indicate that the abnormal energy in the S-wave quasi-stress tensor is much stronger than that in the S-wave particle-velocity. That is because the S-wave quasi-stress tensor is the integral of the S-wave particle-velocity. As time increases, the error accumulates. The S-wave quasi-stress tensor after smooth and median filtering is shown in Figure B-1c. The abnormal energy is removed significantly.

Although we cannot treat the τ_{xx}^S wavefield as the $-\tau_{zz}^S$ wavefield straightforwardly, we can use either of τ_{xx}^{QS} or τ_{zz}^{QS} to generate converted-wave images for geologic structures because both of them have a consistent polarity sign. Thus, the conventional crosscorrelation imaging condition (Claerbout, 1971) can be directly applied to τ^P and τ_{xx}^{QS} (or τ_{zz}^{QS}) wavefields. In the 3D case, even if $\tau_{xx}^{QS} + \tau_{yy}^{QS} + \tau_{zz}^{QS} = 0$, there are three combinations; therefore, the converted-wave images are not unique. In summary, the S-wave quasi-tensor provides a promising solution for converted-wave images in ERTM. But many aspects need further investigation. This area remains as a future research topic.

REFERENCES

- Aki, K., and P. G. Richards, 1980, Quantitative seismology: Theory and methods: W. H. Freeman.
- Balch, A. H., and C. Erdemir, 1994, Sign-change correction for prestack migration of P-S converted wave reflections: Geophysical Prospecting, **42**, 637–663, doi: [10.1111/gpr.1994.42.issue-6](https://doi.org/10.1111/gpr.1994.42.issue-6).
- Baydal, E., D. D. Kosloff, and J. W. C. Sherwood, 1983, Reverse time migration: Geophysics, **48**, 1514–1524, doi: [10.1190/1.1441434](https://doi.org/10.1190/1.1441434).
- Cervený, V., 2001, Seismic ray theory: Cambridge University Press.
- Chang, W. F., and G. A. McMechan, 1986, Reverse-time migration of offset vertical seismic profiling data using the excitation-time imaging condition: Geophysics, **51**, 67–84, doi: [10.1190/1.1442041](https://doi.org/10.1190/1.1442041).
- Chang, W. F., and G. A. McMechan, 1994, 3-D elastic prestack, reverse-time depth migration: Geophysics, **59**, 597–609, doi: [10.1190/1.1443620](https://doi.org/10.1190/1.1443620).
- Chattopadhyay, S., and G. A. McMechan, 2008, Imaging conditions for prestack reverse-time migration: Geophysics, **73**, no. 3, S81–S89, doi: [10.1190/1.2903822](https://doi.org/10.1190/1.2903822).
- Claerbout, J. F., 1971, Toward a unified theory of reflector mapping: Geophysics, **36**, 467–481, doi: [10.1190/1.1440185](https://doi.org/10.1190/1.1440185).
- Collino, F., and C. Tsogka, 2001, Application of the perfectly matched absorbing layer model to

- the linear elastodynamic problem in anisotropic heterogeneous media: *Geophysics*, **66**, 294–307, doi: [10.1190/1.1444908](https://doi.org/10.1190/1.1444908).
- Dellinger, J., and J. Etgen, 1990, Wavefield separation in two-dimensional anisotropic media: *Geophysics*, **55**, 914–919, doi: [10.1190/1.1442906](https://doi.org/10.1190/1.1442906).
- Du, Q., X. Gong, M. Zhang, Y. Zhu, and G. Fang, 2014, 3D PS-wave imaging with elastic reverse-time migration: *Geophysics*, **79**, no. 5, S173–S184, doi: [10.1190/geo2013-0253.1](https://doi.org/10.1190/geo2013-0253.1).
- Du, Q. Z., Y. T. Zhu, and J. Ba, 2012, Polarity reversal correction for elastic reverse time migration: *Geophysics*, **77**, no. 2, S31–S41, doi: [10.1190/geo2011-0348.1](https://doi.org/10.1190/geo2011-0348.1).
- Duan, Y., and P. Sava, 2015, Scalar imaging condition for elastic reverse time migration: *Geophysics*, **80**, no. 4, S127–S136, doi: [10.1190/geo2014-0453.1](https://doi.org/10.1190/geo2014-0453.1).
- Fletcher, R. P., X. Du, and P. J. Fowler, 2009, Reverse time migration in tilted transversely isotropic TTI media: *Geophysics*, **74**, no. 6, WCA179–WCA187, doi: [10.1190/1.3269902](https://doi.org/10.1190/1.3269902).
- Gu, B., Z. Li, X. Ma, and G. Liang, 2015, Multi-component elastic reverse time migration based on the P and S separating elastic velocity-stress equation: *Journal of Applied Geophysics*, **112C**, 62–78, doi: [10.1016/j.jappgeo.2014.11.008](https://doi.org/10.1016/j.jappgeo.2014.11.008).
- Kaelin, B., and A. Guittot, 2006, Imaging condition for reverse time migration: 76th Annual International Meeting and Exposition, SEG, Expanded Abstracts, 2594–2598.
- Kelly, K. R., R. W. Ward, S. Treitel, and R. M. Alford, 1976, Synthetic seismograms: A finite-difference approach: *Geophysics*, **41**, 2–27, doi: [10.1190/1.1440605](https://doi.org/10.1190/1.1440605).
- Li, Z., H. Zhang, Q. Liu, and W. Han, 2007, Numeric simulation of elastic wavefield separation by staggering grid high-order finite-difference algorithm (in Chinese): *Oil Geophysical Prospecting*, **42**, 510–515.
- Ma, D., and G. Zhu, 2003, P- and S-wave separated elastic wave equation numerical modeling (in Chinese): *Oil Geophysical Prospecting*, **38**, 482–486.
- Martin, G. S., R. Wiley, and K. J. Marfurt, 2006, Marmousi2: An elastic upgrade for Marmousi: *The Leading Edge*, **25**, 156–166, doi: [10.1190/1.2172306](https://doi.org/10.1190/1.2172306).
- McMechan, G. A., 1983, Migration by extrapolation of time-dependent boundary values: *Geophysical Prospecting*, **31**, 413–420, doi: [10.1111/gpr.1983.31.issue-3](https://doi.org/10.1111/gpr.1983.31.issue-3).
- Nguyen, B., and G. A. McMechan, 2009, Options for source wavefield reconstruction in prestack reverse-time migration: *Journal of Seismic Exploration*, **18**, 305–314.
- Nguyen, B., and G. A. McMechan, 2012, Excitation amplitude imaging condition for prestack reverse-time migration: *Geophysics*, **78**, no. 1, S37–S46, doi: [10.1190/geo2012-0079.1](https://doi.org/10.1190/geo2012-0079.1).
- Nguyen, B., and G. A. McMechan, 2015, Five ways to avoid storing source wavefield snapshots in 2D elastic prestack reverse time migration: *Geophysics*, **80**, no. 1, S1–S18, doi: [10.1190/geo2014-0014.1](https://doi.org/10.1190/geo2014-0014.1).
- Rocha, D., N. Tanushev, and P. Sava, 2016, Isotropic elastic wavefield imaging using the energy norm: *Geophysics*, **81**, no. 4, S207–S219, doi: [10.1190/geo2015-0487.1](https://doi.org/10.1190/geo2015-0487.1).
- Rosales, D. A., S. Fomel, B. L. Biondi, and P. Sava, 2007, Wave-equation angle-domain common-image gathers for converted waves: *Geophysics*, **73**, no. 1, S17–S26, doi: [10.1190/1.2821193](https://doi.org/10.1190/1.2821193).
- Shabelansky, A. H., A. E. Malcolm, M. C. Fehler, X. Shang, and W. L. Rodi, 2015, Source-independent full wavefield converted-phase elastic migration velocity analysis: *Geophysical Journal International*, **200**, 952–966, doi: [10.1093/gji/ggu450](https://doi.org/10.1093/gji/ggu450).
- Stewart, R. R., J. E. Gaiser, R. J. Brown, and D. C. Lawton, 2003, Converted-wave seismic exploration: Applications: *Geophysics*, **68**, 40–57, doi: [10.1190/1.1543193](https://doi.org/10.1190/1.1543193).
- Sun, R., and G. A. McMechan, 2001, Scalar reverse-time depth migration of prestack elastic seismic data: *Geophysics*, **66**, 1519–1527, doi: [10.1190/1.1487098](https://doi.org/10.1190/1.1487098).
- Sun, R., G. A. McMechan, C. S. Lee, J. Chow, and C. H. Chen, 2006, Pre-stack scalar reverse-time depth migration of 3D elastic seismic data: *Geophysics*, **71**, no. 5, S199–S207, doi: [10.1190/1.2227519](https://doi.org/10.1190/1.2227519).
- Valenciano, A. A., and B. Biondi, 2003, 2-D deconvolution imaging condition for shot-profile migration: 73rd Annual International Meeting, SEG, Expanded Abstracts, P1059–1062.
- Wang, W., and G. A. McMechan, 2015, Vector-based elastic reverse time migration: *Geophysics*, **80**, no. 6, S245–S258, doi: [10.1190/geo2014-0620.1](https://doi.org/10.1190/geo2014-0620.1).
- Wang, W., G. A. McMechan, and Q. Zhang, 2015, Comparison of two algorithms for isotropic elastic P and S decomposition in the vector domain: *Geophysics*, **80**, no. 4, T147–T160, doi: [10.1190/geo2014-0563.1](https://doi.org/10.1190/geo2014-0563.1).
- Whitmore, N. D., 1983, Iterative depth migration by backward time propagation: 53rd Annual International Meeting, SEG, Expanded Abstracts, 382–385.
- Xiao, X., and W. S. Leaney, 2010, Local vertical seismic profiling (VSP) elastic reverse-time migration and migration resolution: Salt-flank imaging with transmitted P-to-S waves: *Geophysics*, **75**, no. 2, S35–S49, doi: [10.1190/1.3309460](https://doi.org/10.1190/1.3309460).
- Yan, J., and P. Sava, 2008, Isotropic angle-domain elastic reverse-time migration: *Geophysics*, **73**, no. 6, S229–S239, doi: [10.1190/1.2981241](https://doi.org/10.1190/1.2981241).
- Yao, D. Z., 1996, A research on reflection and conversion characteristics of several elastic wave recursion equations (in Chinese): *Oil Geophysical Prospecting*, **31**, 467–475.
- Yoon, K., and K. J. Marfurt, 2004, Challenges in reverse-time migration: 74th Annual International Meeting and Exposition, SEG, Expanded Abstracts, 1057–1060.
- Yoon, K., and K. J. Marfurt, 2006, Reverse-time migration using the Poynting vector: *Exploration Geophysics*, **37**, 102–107, doi: [10.1071/EG06102](https://doi.org/10.1071/EG06102).
- Yoon, K., C. Shin, S. Suh, L. R. Lines, and S. Hong, 2003, 3D reverse-time migration using the acoustic wave equation: An experience with the SEG/EAGE data set: *The Leading Edge*, **22**, 38–41, doi: [10.1190/1.1542754](https://doi.org/10.1190/1.1542754).
- Youn, O., and H. W. Zhou, 2001, Depth imaging with multiples: *Geophysics*, **66**, 246–255, doi: [10.1190/1.1444901](https://doi.org/10.1190/1.1444901).
- Zhang, Q., and G. A. McMechan, 2010, 2D and 3D elastic wavefield vector decomposition in the wavenumber domain for VTI media: *Geophysics*, **75**, no. 3, D13–D26, doi: [10.1190/1.3431045](https://doi.org/10.1190/1.3431045).
- Zhang, J., Z. Tian, and C. Wang, 2007, P- and S-wave separated elastic wave equation numerical modeling using 2D staggered-grid: 77th Annual International Meeting, SEG, Expanded Abstracts, 2104–2109.
- Zhang, Y., H. Zhang, and G. Zhang, 2011, A stable TTI reverse time migration and its implementation: *Geophysics*, **76**, no. 3, WA3–WA11, doi: [10.1190/1.3554411](https://doi.org/10.1190/1.3554411).